On Pressure Separation Algorithms (PSepA) for improving the accuracy of incompressible flow simulations

S. Turek, A. Ouazzi, and J. Hron

Institute for Applied Mathematics, University of Dortmund, Germany

Summary. We investigate a new technique called 'pressure separation algorithm' (PSepA) (see [4]) which is able to significantly improve the accuracy of incompressible flow simulations for problems with large pressure gradients. In our numerical studies with the CFD package FEATFLOW (`www.featflow.de`), we mainly focus on low order Stokes elements with nonconforming finite element approximations for the velocity and piecewise constant pressure functions. However, preliminary numerical tests show that this advantageous behavior can be also obtained for higher order discretizations, for instance with Q_2/P_1 finite elements. We analyze the application of this simple, but very efficient algorithm onto several stationary and nonstationary benchmark configurations in 2D and 3D (driven cavity, flow around obstacles), and we demonstrate its effect for spurious velocities in multiphase flow simulations ('static bubble' configuration) if combined with *edge-oriented*, resp., *internal penalty* FEM stabilization techniques.

Key words: Pressure separation, incompressible Navier-Stokes equations

1 Motivation

The improvement of numerical simulation techniques for the incompressible Navier-Stokes equations w.r.t. accuracy, flexibility and robustness still belongs to the important and challenging numerical tasks nowadays. Beside the search for 'better' LBB-stable approximations for pressure and velocity, resp., corresponding stabilization techniques for the numerical treatment of higher Reynolds numbers and for higher order time discretizations, concepts for local adaptivity in space and time belong to the most common techniques which are typically under research. In this paper, we demonstrate as an alternative how to increase the resulting accuracy by a simple trick, namely by 'pressure separation algorithms' (PSepA), which is designed for flow situations which are dominated by the pressure gradient or higher order pressure derivatives.

We illustrate the underlying idea which was originally described in [11] and quite recently in the paper [4] containing numerical results for problems with analytical solutions. To do so, we focus on the (stationary) Navier-Stokes equations for an incompressible fluid in a bounded domain Ω which read

$$\boldsymbol{u} \cdot \nabla \boldsymbol{u} - \nu \Delta \boldsymbol{u} + \nabla p = \boldsymbol{f}, \quad \operatorname{div} \boldsymbol{u} = 0\,. \tag{1}$$

Here, $\boldsymbol{u}$ is the fluid velocity, p the pressure, ν the kinematic viscosity, and $\boldsymbol{f}$ is the body force. Moreover, corresponding boundary conditions on $\partial\Omega$ have to be specified depending on the model problems.

If, as usually, the norm in $(L^2(\Omega))^N, N = 2, 3$, is denoted by $\|\cdot\|_{0,\Omega}$, the norm in $(H^k(\Omega))^N$ by $\|\cdot\|_{k,\Omega}$ and the seminorm in $(H^k(\Omega))^N$ by $|\cdot|_{k,\Omega}$, then the typical velocity error estimation for approximating the Navier-Stokes equations with finite elements of order k for the velocity and (at least) of order $k-1$ for the pressure, can be expressed as follows (see [6])

$$h|\boldsymbol{u} - \boldsymbol{u}_h|_{1,\Omega} + \|\boldsymbol{u} - \boldsymbol{u}_h\|_{0,\Omega} \leq C h^{k+1} \left\{ |\boldsymbol{u}|_{k+1,\Omega} + \tfrac{1}{\nu}|p|_{k,\Omega} \right\}, \tag{2}$$

where $\boldsymbol{u}_h$ is the corresponding finite element approximation of (1). Now, consider instead of (1) the following problem (see [4])

$$\boldsymbol{u} \cdot \nabla \boldsymbol{u} - \nu \Delta \boldsymbol{u} + \nabla \tilde{p} = \boldsymbol{f} - \nabla p_{sep}, \quad \operatorname{div} \boldsymbol{u} = 0, \tag{3}$$

where p_{sep} is a given function, and $\tilde{p} = p - p_{sep}$. Then, the corresponding a priori error estimate [4] reads as follows:

$$h|\boldsymbol{u} - \boldsymbol{u}_{sep,h}|_{1,\Omega} + \|\boldsymbol{u} - \boldsymbol{u}_{sep,h}\|_{0,\Omega} \leq C h^{k+1} \left\{ |\boldsymbol{u}|_{k+1,\Omega} + \tfrac{1}{\nu}|p - p_{sep}|_{k,\Omega} \right\} \tag{4}$$

Consequently, a significant improvement in the (a priori) error estimation is achieved if $\frac{1}{\nu}|p|_{k,\Omega}$ is the dominant term in (2) and if $|p - p_{sep}|_{k,\Omega} \ll |p|_{k,\Omega}$. This situation typically occurs in flow configurations which are dominated by the pressure gradient or for small viscosity parameters such that the choice of p_{sep} as a sufficiently 'good' approximation of the original pressure in (1) is desired. Typical variants for the choice of p_{sep} can be found in [4, 8].

Prototypical flow configurations in single phase CFD simulations, which are candidates for such classes, are problems with singularities which are due to the geometry or boundary conditions. For instance, *driven cavity* problems with pressure singularities (see Fig. 1) in the upper corners due to discontinuous boundary values for the velocity, or *flow around obstacles* settings with large pressure derivatives or even singularities near corners (see Fig. 1) are typical flow settings which are natural candidates for *pressure separation*.

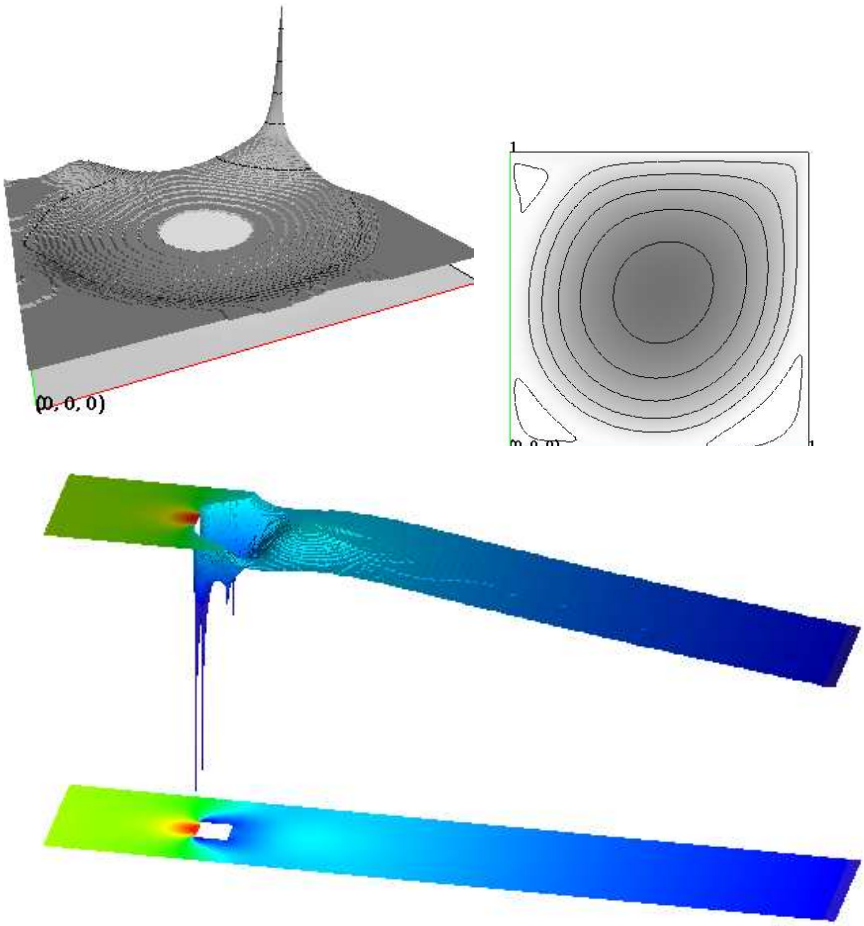

Fig. 1. Singularity of the pressure for the 'Driven Cavity' configuration, together with the streamfunction, and for 'flow around a square'

Another example is multiphase flow with surface tension as local external force which in many cases leads to a discontinuous pressure such that large norms of pressure derivatives naturally appear in the a priori estimate. Moreover, spurious velocities appear near the interfaces - which are not only restricted to such free interface problems (see [5]) - such that the question arises whether pressure separation algorithms can improve the numerical accuracy and robustness in such examples, too. For further improvement of the FEM solution in this case, we use local mesh deformation techniques for grid alignment to accurately calculate the surface tension force and the curvature, and we combine them with edge-oriented FEM stabilization techniques [15] which will essentially help to suppress such spurious oscillations.

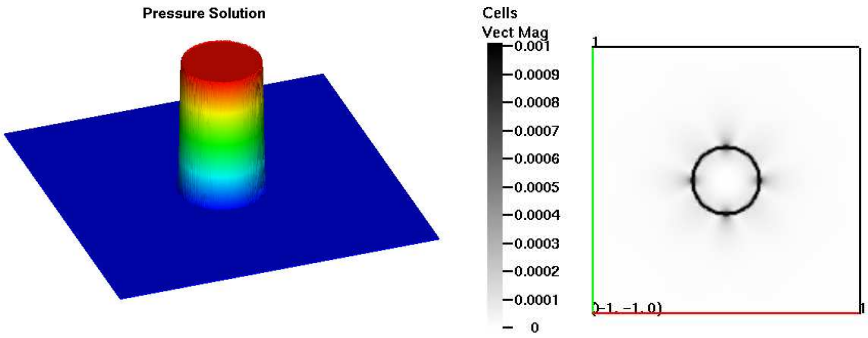

Fig. 2. Pressure and resulting spurious velocity for the 'static bubble' configuration

2 Numerical and algorithmic details

2.1 Discretization aspects

For the discretization, we consider a subdivision $T \in \mathcal{T}_h$ consisting of quadrilaterals/hexahedrals in the domain Ω, and we employ the nonconforming rotated multilinear $\tilde{Q}_1/Q_0$ finite element pair. The nodal values are the mean values of the velocity vector over the element edges, resp., element faces, and the mean values of the pressure over the elements (see [14] for more details).

There are two well-known situations for nonconforming FEM methods when severe numerical problems may arise: Firstly, the lack of coercivity for low order approximations for symmetric deformation tensor formulations, mainly visible for small Re numbers. Secondly, and this for all standard discretization schemes in the case of convection dominated problems, numerical difficulties arise for instance for medium and high Re numbers or for the treatment of pure transport problems: Then, the standard Galerkin formulation fails and may lead to numerical oscillations and to convergence problems of the iterative solvers, too (see [2, 15]). Among the stabilization methods existing in the literature for these types of problems, we use the proposed one in [10, 15] which is based on the penalization of the gradient jumps over element boundaries. In 2D, the additional stabilization term $\mathbf{J}\boldsymbol{u}$, acting only on the velocity $\boldsymbol{u}$ in the momentum equations, takes the following form (with $h_E = |E|$)

$$\langle \mathbf{J}\boldsymbol{u}, \boldsymbol{v} \rangle = \sum_{\text{edge E}} \max(\gamma \nu h_E, \gamma^* h_E^2) \int_E [\nabla \boldsymbol{u}] : [\nabla \boldsymbol{v}] \, d\sigma, \tag{5}$$

and will be simply added to the original bilinear form in order to cure numerical instabilities when computing incompressible flow problems using low order nonconforming finite elements. Moreover, only one generic stabilization term takes care of all mentioned instabilities (see [15]).

The original method presented in (5) was driven by the desire to cure both instabilities for Korn's inequality and convection domination inherent in the approximate solutions. This least-squares term may be interpreted as a continuous high order interior penalty method which can be formulated as a global minimization of the quadratic formulation, derived from the Stokes problem, for instance, with the constraint of the jump of the gradient being equal to zero. So, it can be seen as a manner of filtering the undesired spurious modes in the solution. Moreover, that explains the adequate results in the limit of inviscid flow if the stabilization according to (5) is applied (see [15] for the 'standing vortex' problem). Therefore, the objective is to generalize the mesh-dependent penalty parameter in (5) to provide improvements for two-phase flows with discontinuous pressure, too.

2.2 Algorithmic realization of pressure separation

To reach that the semi-norm $|p - p_{sep}|_k$ is smaller than $|p|_k$, we try to set p_{sep} as approximate solution of the unknown pressure p. This simply can be done by defining p_{sep}, for instance, via appropriate interpolation of the discrete solution p_h from the original problem (1). Then, the complete (stationary) pressure separation algorithm which can be also viewed as basic step inside of a corresponding iterative procedure reads as follows:

1 Step of PSepA:

0. Solve the original problem (1) and obtain $(\boldsymbol{u}_h^0, p_h^0)$

1. Interpolate p_h^0 into any higher order finite element space, at least consisting of piecewise linear, resp., bilinear functions which leads to:

$$p_{sep,h} := I(p_h^0)$$

2. Calculate the new finite element solution of the modified Navier-Stokes equations (3) with $\nabla p_{sep,h}$ as right hand side:

$$(\tilde{\boldsymbol{u}}_h, \tilde{p}_h) := \mathrm{NS}^{-1}(\boldsymbol{f} - \nabla p_{sep,h})$$

3. Set the velocity $\boldsymbol{u}_h = \tilde{\boldsymbol{u}}_h$ and update the pressure p_h:

$$p_h = p_h^0 + \tilde{p}_h$$

If the initial pressure p_h^0 is obtained by solving the original Navier-Stokes equations with $\boldsymbol{f}$ as right hand side, this almost doubles the CPU times. Alternatively, the computation of p_h^0 can be based on an approximation p_{2h} which is obtained in a hierarchical multigrid style on a coarser mesh level $2h$, for instance, or p_h^0 can be directly obtained from a previous Newton-like step

which is typically used in an outer loop for treating the nonlinearity. For a discussion of such variants for computing $p_{sep,h}$, the reader is referred to [4]. Regarding the underlying finite element spaces, in our case the nonconforming Stokes element $\tilde{Q}_1/Q_0$, the intermediate pressure $p_{sep,h}$ is taken as the linear interpolation of p_h into conforming bilinear elements; we also used the interpolation into the nonconforming space $\tilde{Q}_1$ which however gives qualitatively similar results.

Regarding the application of pressure separation in the case of the nonstationary Navier-Stokes equations, the same algorithm could be applied in each time step separately, leading again to a doubling of CPU times. However, there is also the possibility of the following simplification which is based on the idea of extrapolating the pressure in time.

1 Step of nonstationary Pressure Separation:

0. Given $(\boldsymbol{u}_h^{n-1}, p_h^{n-1})$ as solution from time step t^{n-1}

1. Interpolate p_h^{n-1} into any higher order finite element space, at least consisting of piecewise linear, resp., bilinear functions which leads to:

$$p_{sep,h}^n := I(p_h^{n-1})$$

2. Calculate the new finite element solution at time t^n with $\nabla p_{sep,h}^n$ as part of the modified right hand side:

$$(\tilde{\boldsymbol{u}}_h^n, \tilde{p}_h^n) := \mathrm{NS}^{-1}(\boldsymbol{f^n} - \nabla p_{sep,h}^n)$$

3. Set the velocity $\boldsymbol{u}_h^n = \tilde{\boldsymbol{u}}_h^n$ and update the pressure p_h^n:

$$p_h^n = p_h^{n-1} + \tilde{p}_h^n$$

Remark. In step 2., we mean by 'NS^{-1}' the solution of the corresponding generalized stationary Navier-Stokes problem at time step t^n which clearly depends on the chosen time stepping. In our case, we assume a fully coupled, fully implicit approach which however can be easily extended to pressure correction or pressure projection methods. Furthermore, the approximative pressure $p_{sep,h}^n$ can be easily taken as higher order extrapolation in time, for instance via $p_{sep,h}^n = I(2p_h^{n-1} - p_h^{n-2})$ in the case of equidistant time steps which should lead to improved approximation properties due to higher temporal accuracy with almost the same numerical effort.

3 Numerical analysis

The goal of the following examples is to analyze numerically the improvement w.r.t. the resulting accuracy of velocity and pressure via the proposed pressure separation algorithms for several prototypical flow configurations. Here, we restrict our studies to the shown 'simple' variants, that means the subsequent solution of two problems in the steady case and the constant extrapolation of $p^n_{sep,h} = I(p^{n-1}_h)$ backwards in time, in order to show the potential of these approaches regarding the numerical accuracy, not considering the related necessary aspects of numerical efficiency which in the steady test cases can be roughly estimated by a factor of 2.

3.1 Analytical solution

The first example is a two-dimensional test on the unit square for 2 different Reynolds numbers $Re = 1$ and $Re = 1,000$ and analytically given velocity $\boldsymbol{u} = (u_1, u_2)$ and pressure p as defined by the following polynomials:

$$\begin{aligned} u_1(x,y) &= 2x^2(1-x^2)(y(1-y)^2 - y^2(1-y)) \\ u_2(x,y) &= 2y^2(1-y^2)(x(1-x)^2 - x^2(1-x)) \\ p(x,y) &= c(x^3 - y^3 - 0.5) \end{aligned} \tag{6}$$

The constant c is varied to obtain that the corresponding a priori error estimate in (2) is dominated by the pressure gradient and to see its impact onto the accuracy of the computed solution. The right hand side $\boldsymbol{f}$ is chosen such that $(\boldsymbol{u}, p)$ satisfy the stationary Navier-Stokes equations for the given Reynolds numbers. In Table 1, we give the corresponding L^2-norm and H^1-norm of the velocity error and the L^2-norm for the pressure error on different mesh levels: 'Level n' denotes the n-times equidistantly refined unit square. As expected, both the 'high Reynolds number case' as well as the increase of the absolute pressure values have directly influence on the computed velocity error: Firstly, the error scales with the Reynolds number, here $Re = \frac{1}{\nu}$, and secondly, the constant c increases the error since the pressure magnitude and hence its gradient are scaled with c. However, both dependencies influence the error only via the so-called error constant while the asymptotics w.r.t. the mesh size h remains the same. Nevertheless, it is obvious that the velocity errors are significantly improved by the pressure separation algorithm.

Level	$\|\boldsymbol{u}-\boldsymbol{u}_h\|_0$	$\|\boldsymbol{u}-\boldsymbol{u}_h\|_{1,h}$	$\|p-p_h\|_0$	$\|\boldsymbol{u}-\boldsymbol{u}_h\|_0$	$\|\boldsymbol{u}-\boldsymbol{u}_h\|_{1,h}$	$\|p-p_h\|_0$
	without pressure separation			with pressure separation		
			Re=1, c=1			
4	0.01320627	0.21977997	0.04289705	0.00407523	0.07914281	0.0448510
5	0.00332730	0.11060943	0.02138728	0.00093228	0.03681914	0.0219279
6	0.00083443	0.05545565	0.01068082	0.00022132	0.01766485	0.0108244
7	0.00020887	0.02776021	0.00533808	5.3792E-05	0.00863829	0.0053753
8	5.2246E-05	0.01388741	0.00266865	1.3252E-05	0.00426955	0.0026781
9	1.3064E-05	0.00694537	0.00133426	3.2879E-06	0.00212224	0.0013366
			Re=1, c=1,000			
4	10.7625546	173.711219	0.04285851	2.00796426	35.9718175	0.0449270
5	2.93779513	95.2942924	0.02138303	0.38075240	13.6844735	0.0219383
6	0.77022584	50.1414941	0.01068041	0.06983640	5.02810125	0.0108258
7	0.19738275	25.7520552	0.00533804	0.01258139	1.81319313	0.0053754
8	0.04997221	13.0541961	0.00266864	0.00224555	0.64752019	0.0026781
9	0.01257281	6.57264895	0.00133426	0.00039888	0.23009497	0.0013366
			Re=1,000, c=1			
4	2.56237929	27.0587977	0.042775319	0.37903284	6.77388344	0.0453306
5	0.96556353	23.0817867	0.021368298	0.11457742	4.11517335	0.0220339
6	0.34447421	18.6515627	0.010678341	0.03155326	2.27133044	0.0108454
7	0.11699463	13.7212946	0.005337790	0.00775593	1.11769202	0.0053789
8	0.03685431	9.02403558	0.002668620	0.00171123	0.49209582	0.0026787
9	0.01063014	5.36395474	0.001334261	0.00054886	0.19847427	0.0013367
			Re=1,000, c=1,000			
4	264.699897	1185.01441	0.043364293	15.4317586	269.340443	0.0454205
5	147.874546	1122.20719	0.021461306	5.43204942	189.104707	0.0220733
6	76.8259785	1035.76326	0.010691149	1.83832538	131.945249	0.0108609
7	33.1379928	952.824272	0.005339131	0.63121919	90.9434163	0.0053842
8	10.6143169	891.529162	0.002668820	0.21236541	61.2296913	0.0026803
9	3.08294602	827.562355	0.001334310	0.06854484	39.5259910	0.0013371

Table 1. Velocity errors due to $\|\boldsymbol{u}-\boldsymbol{u}_h\|_0$ and $|\boldsymbol{u}-\boldsymbol{u}_h|_1$, pressure error $\|p-p_h\|_0$

3.2 Driven cavity

Driven cavity flows represent a common standard benchmark for incompressible CFD codes and therefore we also present corresponding results for different Reynolds numbers. Furthermore, this problem seems to be an ideal test configuration for the pressure separation since the solution is less regular which is due to the pressure singularity in the corner. We list in Table 2 the kinetic energy, $\frac{1}{2}\int_\Omega \|\boldsymbol{u}\|^2\,dx$, for a regular mesh and for an adapted one near the corners (see Fig. 3). As can be seen in Table 2, almost grid independent results are achieved for the kinetic energy, at least for the PSepA approach. It is also visible that much better results can be obtained on coarse meshes with pressure separation in comparison to the standard approach.

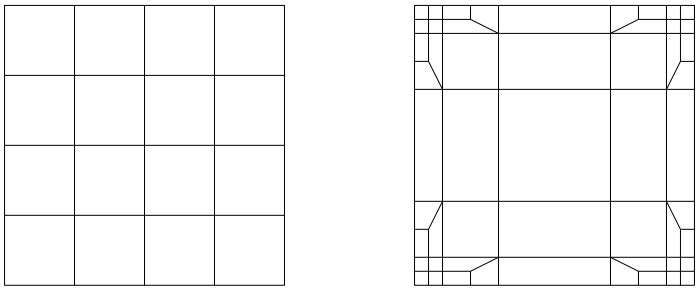

Fig. 3. Two different coarse meshes for 'Driven Cavity'

structured mesh		Energy	Energy
Level	cells	without pressure separation	with pressure separation
		Re=1,000	
4	1024	4.255446720666505E-02	4.809523177616493E-02
5	4096	4.292753746090640E-02	4.582827797164316E-02
6	16384	4.354483303998137E-02	4.484310164052527E-02
7	65536	4.409022680894554E-02	4.459201173310999E-02
8	262144	4.436728290764166E-02	4.453541193883628E-02
9	1048576	4.447217597338023E-02	4.452227397784055E-02
		Re=5,000	
4	1024	4.744206618103668E-02	6.178545053709494E-02
5	4096	4.542745327131271E-02	5.596863706593847E-02
6	16384	4.394207364279471E-02	5.019652320714556E-02
7	65536	4.462170416774443E-02	4.802028792765253E-02
8	262144	4.589567777376605E-02	4.754149961543417E-02
9	1048576	4.677138548602210E-02	4.745519215584770E-02

unstructured mesh		Energy	Energy
Level	cells	without pressure separation	with pressure separation
		Re=1,000	
4	3392	3.937830914695982E-02	4.258603278981851E-02
5	13568	4.200638598599166E-02	4.399538203747823E-02
6	54272	4.343367659646590E-02	4.442539201306887E-02
7	217088	4.410374815761506E-02	4.451194162495991E-02
8	868352	4.437769488742017E-02	4.452067552798117E-02
9	3473408	4.447552512831641E-02	4.451922842679222E-02
		Re=5,000	
4	3392	3.694454761504827E-02	4.478929109363260E-02
5	13568	3.875516662905162E-02	4.519893868737240E-02
6	54272	4.160819937746986E-02	4.621377280452104E-02
7	217088	4.428310545723057E-02	4.712166739526875E-02
8	868352	4.596571822224903E-02	4.741444989451889E-02
9	3473408	4.683499558639783E-02	4.745377227286869E-02

Table 2. Driven cavity results for Re=1,000 and 5,000

3.3 Flow around obstacles

Flow around obstacles of different shape is another adequate configuration to analyze the effectiveness of pressure separation not only w.r.t. the accuracy of the velocity, but also regarding the pressure since the quantities of interest are the lift C_{lift} and the drag C_{drag} coefficients

$$C_{lift} = -C \int_S (\nu \frac{\partial \boldsymbol{v}_t}{\partial \boldsymbol{n}} \boldsymbol{n}_x + p\boldsymbol{n}_y)\, ds, \quad C_{drag} = C \int_S (\nu \frac{\partial \boldsymbol{v}_t}{\partial \boldsymbol{n}} \boldsymbol{n}_y - p\boldsymbol{n}_x)\, ds, \quad (7)$$

where S is the contact line, resp., area of the obstacle with the fluid, and C is a scaling constant. The computation of the surface integrals in (7) can be also obtained via related volume integrals due to the weak formulations in FEM approaches. We consider functions $\boldsymbol{v}_d \in (H^1(\Omega))^N$ and $\boldsymbol{v}_l \in (H^1(\Omega))^N$ with

$$\boldsymbol{v}_{d|S} = (e_1, 0)^T,\ \boldsymbol{v}_{d|\bar{\Omega}-S} = \boldsymbol{0} \quad \text{and} \quad \boldsymbol{v}_{l|S} = (0, e_2)^T,\ \boldsymbol{v}_{l|\bar{\Omega}-S} = \boldsymbol{0} \quad (8)$$

where e_i is the i^{th} component of the unity. Then, the corresponding expression via volume integrals reads [9]

$$\begin{array}{l} C_{lift} \ = -C((\nu\nabla\boldsymbol{u}, \nabla\boldsymbol{v}_l) - (p, \nabla\cdot\boldsymbol{v}_l)) \\ C_{drag} = -C((\nu\nabla\boldsymbol{u}, \nabla\boldsymbol{v}_d) - (p, \nabla\cdot\boldsymbol{v}_d)) \end{array} \quad (9)$$

with $(\cdot,\cdot)$ denoting the inner product in $(L^2(\Omega))^N$, $N = 2, 3$. This problem corresponds to well-known benchmark configurations and has been described in [14, 16]. Two different obstacles, a cylinder with circular and with square cross-section, are considered in two and three dimensions. The coarse meshes for the two-dimensional case are shown in Fig. 4, while the corresponding 3D coarse mesh is derived from the 2D grid by extrusion in z-direction with equidistant layers.

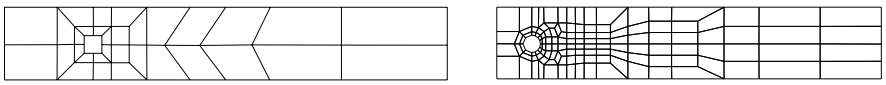

Fig. 4. Coarse meshes for the 'flow around obstacle' configurations in 2D

In the case of flow around the 2D cylinder, the solution is quite smooth and not dominated by the pressure gradient which seems to be the reason that the pressure separation algorithm does not essentially improve the solution quality, at least for the low Reynolds number cases $Re = 20$ and $Re = 50$. However, in the three-dimensional case [1, 9], the pressure separation brings significantly more improvement to the solution, particularly for the lift coefficient (see Table 4).

Force Level	cells	C_{drag} without pressure separation	C_{lift} without pressure separation	C_{drag} with pressure separation	C_{lift} with pressure separation
Re=20 / reference values: $C_D = 5.580$, $C_L = 0.0106$					
3	4264	0.56012E+01	0.96490E-02	0.56206E+01	0.10498E-01
4	16848	0.55803E+01	0.10143E-01	0.55703E+01	0.10350E-01
5	66976	0.55789E+01	0.10435E-01	0.55707E+01	0.10462E-01
6	267072	0.55793E+01	0.10559E-01	0.55747E+01	0.10548E-01
7	1066624	0.55795E+01	0.10601E-01	0.55771E+01	0.10588E-01
8	4263168	0.55795E+01	0.10614E-01	0.55783E+01	0.10605E-01
Re=50 / reference values: $C_D = 3.694$, $C_L = -0.0107$					
3	4264	0.38109E+01	-0.11007E-01	0.38136E+01	-0.11184E-01
4	16848	0.37237E+01	-0.10959E-01	0.37041E+01	-0.11045E-01
5	66976	0.37013E+01	-0.10794E-01	0.36897E+01	-0.10860E-01
6	267072	0.36961E+01	-0.10749E-01	0.36908E+01	-0.10786E-01
7	1066624	0.36949E+01	-0.10741E-01	0.36925E+01	-0.10758E-01
8	4263168	0.36946E+01	-0.10739E-01	0.36935E+01	-0.10747E-01

Table 3. ***Flow around a 2D cylinder***: Drag and lift coefficient with and without pressure separation technique

Force Level	cells	C_{drag} without pressure separation	C_{lift} without pressure separation	C_{drag} with pressure separation	C_{lift} with pressure separation
3	6144	0.59160E+01	-0.12441E-02	0.61155E+01	0.32743E-02
4	49152	0.61549E+01	0.47570E-02	0.61447E+01	0.80229E-02
5	393216	0.61829E+01	0.77422E-02	0.61602E+01	0.91252E-02
6	3145728	0.61861E+01	0.87470E-02	0.61721E+01	0.93316E-02
reference value		$C_{drag} = 6.185, C_{lift} = 0.00940$			

Table 4. ***Flow around a 3D cylinder***: Lift and drag coefficient with and without pressure separation technique for $Re = 20$

This situation changes completely in the case of the flow around the square, already in 2D as well as in 3D, which leads to pressure singularities near the corners of the interior square such that the application of pressure separation is getting significantly more advantageous.

Force Level	cells	C_{drag} without pressure separation	C_{lift} without pressure separation	C_{drag} with pressure separation	C_{lift} with pressure separation
Re=20/ reference values: $C_D = 6.47$, $C_L = 0.0712$					
3	512	0.64522E+01	0.74753E-01	0.68402E+01	0.84024E-01
4	2048	0.63551E+01	0.70146E-01	0.65059E+01	0.73883E-01
5	8192	0.63864E+01	0.69694E-01	0.64587E+01	0.71458E-01
6	32768	0.64239E+01	0.70204E-01	0.64640E+01	0.71122E-01
7	131072	0.64463E+01	0.70646E-01	0.64705E+01	0.71153E-01
8	524288	0.64572E+01	0.70908E-01	0.64728E+01	0.71201E-01
9	2097152	0.64624E+01	0.71039E-01	0.64726E+01	0.71217E-01
Re=50/ reference values: $C_D = 4.14$, $C_L = 0.0239$					
3	512	0.43589E+01	0.31870E-01	0.45827E+01	0.38136E-01
4	2048	0.42174E+01	0.24908E-01	0.42779E+01	0.26107E-01
5	8192	0.41397E+01	0.23774E-01	0.41619E+01	0.24433E-01
6	32768	0.41223E+01	0.23730E-01	0.41385E+01	0.24202E-01
7	131072	0.41248E+01	0.23796E-01	0.41381E+01	0.24102E-01
8	524288	0.41296E+01	0.23830E-01	0.41396E+01	0.24012E-01
9	2097152	0.41328E+01	0.23846E-01	0.41399E+01	0.23951E-01

Table 5. ***Flow around a 2D square***: Drag and lift coefficient with and without pressure separation technique

Force Level	cells	C_{drag} without pressure separation	C_{lift} without pressure separation	C_{drag} with pressure separation	C_{lift} with pressure separation
3	8192	0.76277E+01	0.38110E-01	0.77676E+01	0.52552E-01
4	65536	0.77550E+01	0.54334E-01	0.77247E+01	0.63255E-01
5	524288	0.77438E+01	0.63013E-01	0.77342E+01	0.67294E-01
6	4194304	0.77447E+01	0.67372E-01	0.77556E+01	0.68589E-01
reference value		$C_{drag} = 7.76, C_{lift} = 0.0688$			

Table 6. ***Flow around a 3D square***: Lift and drag coefficient with and without pressure separation technique for $Re = 20$

Finally, the nonstationary case of periodically oscillating flow for a medium Reynolds number is also considered and the results are plotted in Fig. 5. For the 2D flow around cylinder, the Reynolds number is increased to $Re = 100$, with the aim to examine the resulting effects. The time discretization is based on the classical Crank-Nicolson method, and a fully coupled, fully implicit treatment is used (see [14] for more details). In this nonstationary case, that means the case of higher Re number, the pressure separation algorithm clearly improves the solution for both lift amplitude and frequency. However, since we perform the described constant extrapolation in time only, the results are depending on the actual time step size, too. So, more numerical investigations are required to explore the various described variants of the PSepA algorithms to check the numerical behavior w.r.t. accuracy and efficiency.

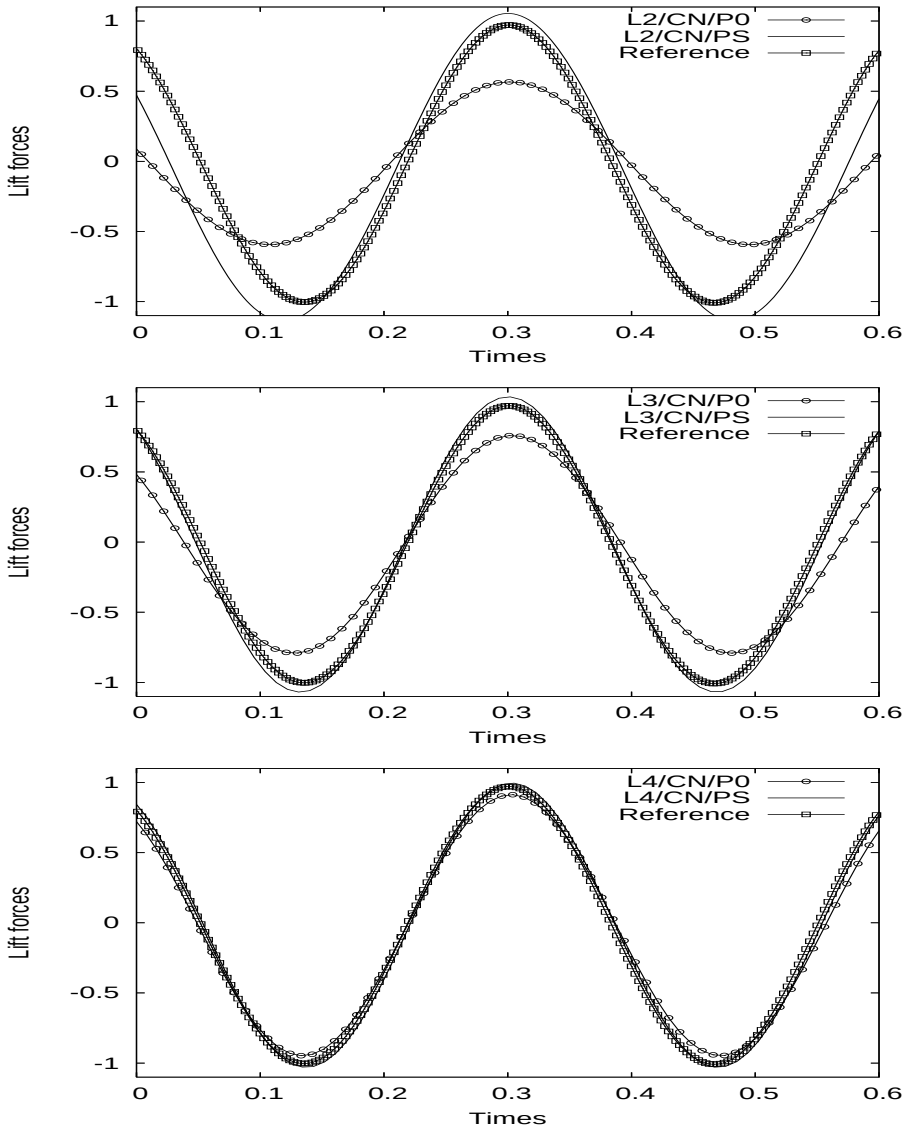

Fig. 5. Lift coefficient for various mesh levels ('L=2-4') for Crank-Nicolson 'CN' as time-stepping scheme with pressure separation 'PS' and without pressure separation 'P0'

3.4 Static bubble

In the next step, we illustrate the robustness and efficiency of the pressure separation algorithm, and of the described edge-oriented FEM stabilization, for flows with interfaces which naturally lead to large pressure derivatives. Due to its simplicity, but nevertheless due to its prototypical behavior for multiphase flow models, we consider a stationary bubble at equilibrium, something that holds for the slow motion of a gas bubble in a viscoplastic fluid (for instance, see [3]). Since the bubble is at rest, we should have a zero velocity field; unfortunately, most numerical methods generate spurious currents, as for instance reported in [5, 12] (see also Fig. 2).

In our test case, we restrict the simulation to the configuration proposed in [13, 7] which is a circular bubble with radius $r = 0.25$ positioned in the center of a unit square. The coefficient of surface tension σ and all viscosities were set to unity. Then, according to the Laplace-Young law, the pressure inside the bubble p_i and the outside pressure p_o satisfy:

$$p_i = p_o + \sigma/r \tag{10}$$

Two different meshes with identical number of mesh cells, and hence degrees of freedom, are considered (see Fig. 6), namely an equidistant and a locally adapted mesh by concentrating the grid points in the vicinity of the interface where the pressure exhibits a discontinuity. Consequently, the aligned mesh should resolve the interface in a much better way, while preserving the connectivity of the grid topology for efficiency reasons. Table 7 and 8 show the resulting errors of the velocity and pressure for the different methods which will be discussed in the subsequent part of the paper.

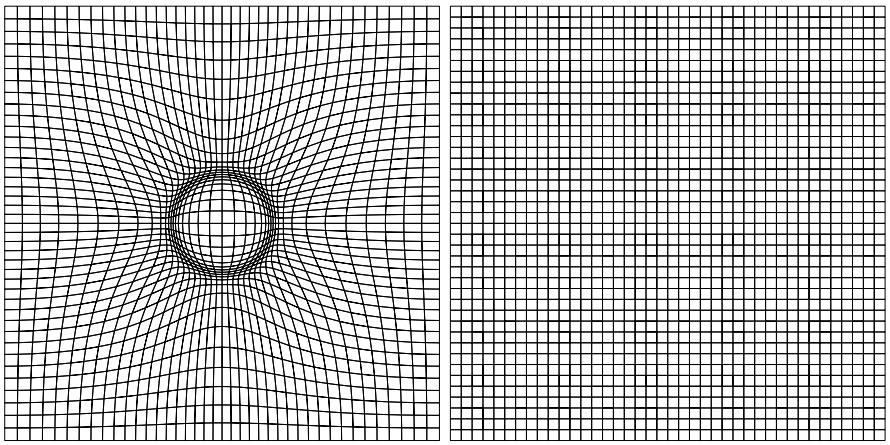

Fig. 6. Adapted vs. 'simple' mesh (both $NEL = 1,600$) on mesh level 4

Level	without pressure separation $\lvert p_i - p_o\rvert/(\frac{\sigma}{r})$	$\lVert \boldsymbol{u} - \boldsymbol{u}_h\rVert_0$	$\lvert \boldsymbol{u} - \boldsymbol{u}_h\rvert_{1,h}$	NL/MG	with pressure separation $\lvert p_i - p_o\rvert/(\frac{\sigma}{r})$	$\lVert \boldsymbol{u} - \boldsymbol{u}_h\rVert_0$	$\lvert \boldsymbol{u} - \boldsymbol{u}_h\rvert_{1,h}$	NL/MG
without edge-oriented FEM								
4	0.954349	0.002608	0.207652	5/1	0.992366	0.001552	0.118638	5/1
5	0.979682	0.000971	0.153784	5/1	0.997579	0.000607	0.091726	5/1
6	0.992961	0.000362	0.112884	4/1	1.001254	0.000237	0.069493	4/1
7	0.997166	0.000138	0.082118	4/1	1.001094	0.000097	0.051485	4/1
with global edge-oriented FEM with penalty parameter $\gamma = 10$								
4	0.9520738	3.33E-05	0.002560	6/1	0.989788	2.47E-05	0.001871	6/1
5	0.9792187	1.21E-05	0.001819	5/1	0.997226	9.97E-06	0.001452	5/1
6	0.9926422	4.71E-06	0.001406	5/1	1.001089	3.86E-06	0.001126	5/1
7	0.9966825	1.72E-06	0.001030	4/1	1.000645	1.37E-06	0.000801	4/1
with global edge-oriented FEM with penalty parameter $\gamma = 1,000$								
4	0.951998	3.38E-07	2.60E-05	6/1	0.988809	2.20E-07	1.64E-05	6/1
5	0.979198	1.23E-07	1.84E-05	5/1	0.997101	8.06E-08	1.16E-05	5/1
6	0.992635	4.78E-08	1.42E-05	5/1	1.001279	3.21E-08	9.07E-06	5/1
7	0.996678	1.75E-08	1.04E-05	4/1	1.000998	1.25E-08	6.46E-06	4/1
with edge-oriented FEM with local penalty parameter γ as a function of the distance to the interface								
4	0.949683	3.61E-07	2.68E-05	6/1	0.986366	2.40E-07	1.75E-05	6/1
5	0.978834	1.19E-07	1.73E-05	5/1	0.996440	9.04E-08	1.25E-05	5/1
6	0.992673	4.75E-08	1.31E-05	5/1	1.000876	3.74E-08	9.68E-06	5/1
7	0.996931	2.01E-08	9.56E-06	4/1	1.000757	1.67E-08	6.85E-06	4/1

Table 7. ***Equidistant mesh***: Errors of pressure and velocity as well as total number of nonlinear iterations and averaged number of multigrid steps per nonlinear iteration (NL/MG) to gain 1 digit

Level	without pressure separation $\lvert p_i - p_o\rvert/(\frac{\sigma}{r})$	$\lVert \boldsymbol{u} - \boldsymbol{u}_h\rVert_0$	$\lvert \boldsymbol{u} - \boldsymbol{u}_h\rvert_{1,h}$	NL/MG	with pressure separation $\lvert p_i - p_o\rvert/(\frac{\sigma}{r})$	$\lVert \boldsymbol{u} - \boldsymbol{u}_h\rVert_0$	$\lvert \boldsymbol{u} - \boldsymbol{u}_h\rvert_{1,h}$	NL/MG
without edge-oriented FEM								
4	1.000669	1.89E-04	0.097654	6/1	1.001900	1.74E-04	0.041707	6/1
5	1.000135	3.50E-05	0.057960	5/1	1.000983	5.67E-05	0.032685	5/1
6	1.000032	6.62E-06	0.037825	4/1	1.000322	1.89E-05	0.023153	3/1
7	1.000000	2.25E-06	0.028948	4/1	1.000140	6.48E-06	0.016411	4/1
with global edge-oriented FEM with the penalty parameter $\gamma = 10$								
4	1.000719	1.87E-05	0.004474	5/1	1.000829	1.55E-05	0.003341	5/1
5	1.000336	4.21E-06	0.002285	4/2	1.000513	5.34E-06	0.002529	4/2
6	1.000109	1.66E-06	0.001819	4/2	1.000136	2.05E-06	0.002013	4/2
7	1.000040	5.36E-07	0.001158	4/2	1.000044	6.51E-07	0.001282	4/2
with global edge-oriented FEM with the penalty parameter $\gamma = 1,000$								
4	1.000712	2.18E-07	5.11E-05	5/1	1.000650	1.81E-07	3.81E-05	5/1
5	1.000347	5.25E-08	2.71E-05	4/2	1.000465	6.21E-08	2.86E-05	4/2
6	1.000113	2.13E-08	2.19E-05	4/2	1.000119	2.43E-08	2.30E-05	4/2
7	1.000043	6.80E-09	1.37E-05	4/2	1.000035	7.65E-09	1.45E-05	4/2
with edge-oriented FEM with local penalty parameter γ as a function of the distance to the interface								
4	1.000599	5.22E-07	1.08E-04	6/1	1.000828	4.95E-07	8.88E-05	5/1
5	1.000277	1.99E-07	8.52E-05	4/2	1.000061	1.72E-07	6.96E-05	4/2
6	0.999927	7.07E-08	6.24E-05	5/2	0.999786	7.31E-08	5.87E-05	5/2
7	1.000017	2.60E-08	4.29E-05	4/2	0.999927	2.46E-08	3.81E-05	4/2

Table 8. ***Aligned mesh***: Errors of pressure and velocity as well as total number of nonlinear iterations and averaged number of multigrid steps per nonlinear iteration (NL/MG) to gain 1 digit

It is obvious that improved results via the pressure separation algorithm are mainly obtained for the pressure on the equidistant meshes, while on the locally aligned meshes no significant improvements via PSepA are visible since the local alignment itself improves already the pressure error drastically. Moreover, the improvement in the velocity error is almost negligible, particularly to eliminate the spurious currents. Again, the velocity error is significantly improved by adapting the mesh towards the interface via the grid deformation algorithm. So, the local grid alignment provides a more precise approximation of the interface, and correspondingly much better results for the pressure, and also for the velocity, are shown in Table 8. However, the limitation of pressure separation to improve the spurious velocity modes remains: Neither pressure separation nor the grid deformation are able to eliminate totally the spurious velocity.

This is in contrast to the additional (local) stabilization of the momentum equations via the described edge-oriented FEM approach for this type of problems: The results for the velocity improve dramatically, and the error seems to be proportionally decreasing with the order of the mesh-dependent penalty parameter. As a main result, the spurious velocity currents are significantly diminished for both types of meshes. Moreover, increasing the magnitude of the (globally defined) mesh-dependent penalty parameter does not degrade the performance of the nonlinear, resp., linear solvers.

Taking into account our previous studies for edge-oriented FEM stabilization [10, 15], in the next step the mesh-dependent penalty parameter is defined not only as a global constant, but also as local function which takes into account the position of the interface (compare with (5))

$$\sum_{\text{edge E}} \max(\gamma\nu h_E, \gamma^* h_E^2, \gamma_{\text{dist}} f(dist(\Gamma); h_E) h_E) \int_E [\nabla \boldsymbol{u}] : [\nabla \boldsymbol{v}] d\sigma$$

with a sufficiently large constant $\gamma_{\text{dist}} \gg 0$, a distance function $dist(\Gamma)$ w.r.t. the interface, and f defined as a variant of the Dirac function. Since for problems with free interfaces, the numerical perturbations occur in most cases around the interface, there a high value of the mesh-dependent penalty parameter is required. Away from the interface, the parameters should be designed so that the penalty parameter remains in accordance with the older settings as explained before. Therefore, the mesh-dependent penalty function was defined to be inversely proportional to the distance which can be obtained, for instance, via a standard level set function as global distant measure. However, these settings require much more and careful numerical analysis, in particular in combination with FEM level set techniques for free interface problems which will be addressed in a forthcoming paper.

4 Conclusion

In this paper we have dealt with a new class of pressure separation algorithms (PSepA) for incompressible flow problems which may essentially improve the obtained approximation properties of velocity and pressure in such cases where high pressure derivatives together with small viscosity parameters are dominating the a priori error estimate. In particular for configurations with large pressure gradients due to the geometry or the applied boundary conditions, the theoretical results are confirmed via the resulting numerical tests, and this for 2D as well as 3D configurations with steady and time-dependent flow behavior. Moreover, we investigated numerically a problem which is prototypical for free interface, resp., multiphase problems where pressure discontinuities and also spurious velocities arise. While PSepA can essentially improve the pressure approximation, the combination with edge-oriented FEM stabilization seems to eliminate the spurious currents, (almost) independent of the mesh resolution. In this case, the edge-oriented FEM stabilization is applied with a global as well as a local mesh-dependent penalty parameter which leads to very promising results.

It is clear that further investigation is necessary, particularly to examine some different variations of the pressure separation algorithms, also w.r.t. higher order finite element spaces or other discretization types, for instance in the Finite Volume setting. Moreover, the application of the examined special edge-oriented FEM stabilization to general multiphase problems in conjunction with local mesh adaptation, and its interplay with dynamic effects have to be numerically studied and analyzed in future. However, the presented results for the pressure separation algorithms are very promising due to their simplicity and efficiency, and also due to their high flexibility regarding very different discretization and solver types, such that much more extensive tests for more realistic flow situations should be performed as soon as possible.

References

[1] Braack, M. and Richter, T. Solutions of 3d navier-stokes benchmark problems with adaptive finite elements. *Computers and Fluids*, 35(4):372–392, 2006.

[2] Burman, E. and Hansbo, P. A stabilized non-conforming finite element method for incompressible flow. *Comput. Methods. Appl. Mech. Engrg.*, 195 (23-24):2881–2899, 2006.

[3] Dubash, N. and Frigaard, I. Conditions for static bubbles in viscoplastic fluids. *Physics of Fluids*, 16:4319–4330, 2004.

[4] Ganesan, S. and John, V. Pressure separation: a technique for improving the velocity error in finite element discretisations of the Navier-Stokes equations. *Applied Mathematics and Computation*, 165:275–290, 2005.

[5] Ganesan, S., Matthies, G., and Tobiska, L. On spurious velocities in incompressible flow problems with interfaces. *Comput. Methods Appl. Mech. Engrg.*, 196:1193–1202, 2007.

[6] Girault, V. and Raviart, P. A. *Finite Element Methods for Navier-Stokes equations*. Springer, 1986. Berlin-Heidelberg.

[7] S. Hysing. A new implicit surface tension implementation for interfacial flows. *International Journal for Numerical Methods in Fluids*, 51:659–672, 2006.

[8] Jian-Guo Liu, Jie Liu, and Robert L. Pego. Divorcing pressure from viscosity in incompressible Navier-Stokes dynamics. Preprint CSCAMM-05-01, University of Maryland, 2005.

[9] John, V. Higher order finite element methods and multigrid solvers in a benchmark problem for the 3-D Navier-Stokes equations. *Int. J. Numer. Meth. Fluids*, 40:775–798, 2002.

[10] Ouazzi, A. *Finite Element Simulation of Nonlinear Fluids. Application to Granular Material and Powder*. Shaker Verlag, 2006. ISBN 3-8322-5201-0.

[11] Schieweck, F. *Parallele Lösung der stationären inkompressiblen Navier-Stokes Gleichungen*. Otto-von-Guericke-Universität Magdeburg, Fakultät für Mathematik, 1997. Habilitation.

[12] Shirani, E., Ashgriz, N., and Mostaghimi, J.E. Interface pressure calculation based on conservation of momentum for front capturing methods. *Journal of Computational Physics archive*, 203:154–175, 2005.

[13] Smolianski, A. *Numerical Modeling of Two-Fluid Interfacial Flows*. University of Jyvaskyla, 2001. PhD thesis, ISBN 3-8322-5201-0.

[14] Turek, S. *Efficient solvers for incompressible flow problems: An algorithmic and computational approach*. Springer, 1999. LNCSE 6.

[15] Turek, S. and Ouazzi, A. Unified edge–oriented stabilization of nonconforming finite element methods for incompressible flow problems: Numerical investigations. *JNM*, 2007. in press.

[16] Turek, S. and Schäfer, M. Benchmark computations of laminar flow around cylinder. In E. H. Hirschel, editor, *Flow Simulation with High-Performance Computers II*, volume 52 of *Notes on Numerical Fluid Mechanics*, pages 547–566. Vieweg, 1996. co. F. Durst, E. Krause, R. Rannacher.